ORIGINAL RESEARCH PAPER

Structural and mechanical properties of AFe_2O_4 (A = Zn, $Cu_{0.5}Zn_{0.5}$, $Ni_{0.3}Cu_{0.2}Zn_{0.5}$) nanoparticles prepared by citrate method at low temperature

***Ahmad Gholizadeh** **

School of Physics, Damghan University (DU), Damghan, I.R. Iran

Received: 2017-08-21 Accepted: 2017-11-16 Published: 2018-03-20

ABSTRACT

In this work, the structural and elastic moduli properties of $ZnFe_2O_4$, $Zn_{0.5}Cu_{0.5}Fe_2O_4$, and $Ni_{0.3}Cu_{0.2}Zn_{0.5}Fe_2O_4$ ferrites prepared by the citrate method have been investigated. The structural characterization of the samples is evidence for a cubic structure with Fd-3m space group. The Halder-Wagner analysis was used to study crystallite sizes and lattice strain and also stress and energy density. The cation distribution for each composition has been suggested. The experimental and theoretical lattice constants were found to be in good agreement with each other confirming the agreeability of the suggested cation distribution. The force constants for tetrahedral and octahedral sites have been determined by infrared spectral analysis. The increase in force constants of $ZnFe_2O_4$ nanoparticles compared to other samples suggests the elastic properties of this sample is better than the other samples. The values of Young's modulus, rigidity modulus, bulk modulus, Debye temperature have been determined. In addition, using the values of the compliance s_{ij} obtained from elastic stiffness constants, the values of Young's modulus and Poisson's ratio along the oriented direction have been calculated for the samples. Consequently, we can conclude the $ZnFe_2O_4$ nanoparticles could be more useful in industrial applications because of their elastic properties compared to other samples.

Keywords: *Ferrites; Citrate method; X-ray diffraction method; IR spectroscopy; Mechanical properties.*

How to cite this article

Gholizadeh A. Structural and Mechanical Properties of AFe_2O_4 (A = Zn, $Cu_{0.5}Zn_{0.5}$, $Ni_{0.3}Cu_{0.2}Zn_{0.5}$) Nanoparticles Prepared by Citrate Method at Low Temperature. J. Nanoanalysis., 2018; 5(1): 7-16. DOI: 10.22034/jna.2018.541845

INTRODUCTION

Soft ferrites have been widely used for different kinds of magnetic devices such as inductors, transformers and magnetic heads for high frequency as their electrical resistivity is higher than those of soft magnetic alloys. Ferrite structure with chemical formula AB_2O_4 was recognized to be an array of oxide anions with two interstitial cation sites A (tetrahedral) and B (octahedral) sublattices [1]. A and B are divalent and trivalent elements, respectively. The proper elemental selection and occupancy of these sites drastically modify the corresponding physical property. Such modification is attributed to the surroundings generated crystal field. AB_2O_4 crystallizes at ambient conditions in the cubic spinel structure of space group Fd-3m with 8 f.u. in the conventional unit cell. The cubic unit cell is formed by 56 atoms, 32 oxygen anions distributed in a cubic close-

* Corresponding Author Emails: gholizadeh@du.ac.ir; ah_gh1359@yahoo.com Tel: +98(23)35220090

packed structure, and 24 cations occupying 8 of the 64 available tetrahedral sites (A sites) and 16 of the 32 available octahedral sites (B sites) [1].

There are three configurations for the ferrite cation distribution; normal, inverse and mixed spinels. Nickel ferrite ($NiFe_2O_4$) and copper ferrite ($CuFe_2O_4$) have an inverse spinel structure with Ni^{2+} and Cu^{2+} ions at octahedral B sites and Fe^{3+} ions are equally distributed at tetrahedral A and octahedral B sites. The ferric ions preferentially fill all of the eight A-sites. The remaining eight go on to the B sites, as do the eight Ni^{2+} ions. The antiferromagnetic interaction orients these eight Fe^{3+} moments and eight nickel moments antiparallel to the eight Fe^{3+} moments on the tetrahedral sites. The Fe^{3+} ion moments will just cancel, but the moments on the nickel ions give rise to an uncompensated moment or magnetization. On the other hand, zinc ferrite ($ZnFe_2O_4$) has a normal spinel structure with Zn^{2+} ions at A sites and Fe^{3+} ions at B-sites. Because of the preferences of Zn^{2+} to occupy the tetrahedral spinel sites forming a normal spinel, while Cu^{2+} occupies mainly the octahedral [B] sites, and thus, the tetrahedral sites are occupied by half of Fe^{3+} and $CuFe_2O_4$ describes as fully inverse spinel. In the case of $Zn_{1-x}Cu_xFe_2O_4$, where $0 < x < 1$, the tetrahedral sites are occupied both by Zn^{2+} and Fe^{3+} cations and this spinel structure are denoted as partially inverse [2].

The $Zn_{1-x}Cu_xFe_2O_4$ have been widely studied for their intriguing magnetic and catalytic properties and also for their chemical reactivity. Nowadays, Ni-Cu-Zn ferrites have been the dominant materials for Multi-Layer Chip Capacitors (MLCC) and Multi-Layer Chip Inductor (MLCI) due to its better magnetic properties at high frequency and low sintering temperature [3].

Studies of the elastic constants are important in order to understand the behavior of the engineering materials. Elastic constants related closely to many physical properties of solids, such as acoustic–phonon frequencies, internal stress, Debye temperature, etc. Furthermore, they provide a sensitive probe of phase transitions and an indication of the nature of interatomic and interionic binding forces in the material [4,5]. Further, the elastic properties of Fe_3O_4 could be important in industrial applications because of their elastic data are very much useful to determine the strength of the materials under various strained conditions. While in basic research, the data are useful obtaining an insight into the structure.

The ultrasonic pulse transmission technique is the most convenient technique for elastic constants and Debye temperature determination [5]. To study the elastic properties of spinel ferrite and garnet systems, a new technique based on the infrared spectroscopy has been developed by Modi et al. [6]. The IR spectra absorption bands mainly appear due to the vibrations of the oxygen ions with the cations producing various frequencies in the unit cell. In certain mixed ferrite materials, as the concentration of the divalent metal ions increases, it gives rise to the structural change or the cations distribution in spinel lattice crystal without affecting the spinel ferrite structure [1]. The structural changes brought by the metal ions that are either lighter or heavier than divalent ions in the ferrites strongly influence the lattice vibration. Also, the vibration frequency depends on the cations' mass, oxygen distance and the bonding force [5].

There are two ways of expressing the elastic properties of crystals, one in terms of elastic stiffness constants, usually denoted by C_{ij}, where i and j may have the values 1 to 6, and the other in terms of the elastic compliance constants, S_{ij}. In general, there are 36 elastic constants, but in the case of isotropic and homogeneous materials like spinel ferrite and garnet, the elastic stiffness constants can be reduced to three (C_{11}, C_{12} and C_{44}). The crystal to be compressed or stretched in various directions so that only one component of strain is produced, e.g. a uniform expansion parallel to the x-axis. Usually, to obtain such a change of shape it is necessary to apply simultaneously stretching forces of unequal amount parallel to all three axes. The constant c_{11}, is the ratio under these conditions of the stretching force parallel to the x-axis, to the expansion in that direction. The inverse of the elastic stiffness constant tensor, often called the compliance constants tensor, with components can be used to derive the linear compressibilities along the principal axes of the coordinate system.

In this paper, it is tried to explain the structural and elastic properties of AFe_2O_4 (A=Zn, Zn-Cu, Zn-Cu-Ni) nanoparticles prepared by citrate methods which have been not investigated so far. These compounds have long been the subject of study because of its technological applications as compared to the other ferrites. The strain due to lattice deformation of the samples was estimated by Scherer and Halder-Wagner (H-W) methods. In addition, the elastic moduli properties of the samples have been specified by using a new technique based on the infrared spectroscopy.

Finally, the structural and elastic properties of the samples have been compared.

EXPERIMENTAL

Materials and sample preparation

The $ZnFe_2O_4$, $Zn_{0.5}Cu_{0.5}Fe_2O_4$ and $Ni_{0.3}Cu_{0.2}Zn_{0.5}Fe_2O_4$ ferrites were prepared by the citrate precursor method and similar to the recipe reported elsewhere [7-9]. Firstly, a solution containing appropriate concentrations of metal nitrates $Fe(NO_3)_3{\cdot}9H_2O$, $Zn(NO_3)_2{\cdot}4H_2O$, $Cu(NO_3)_2{\cdot}3H_2O$, $Ni(NO_3)_2{\cdot}6H_2O$, and citric acid, equal to the total number of moles of nitrate ions and according to Table 1 was evaporated at 50°C, overnight. The homogeneous sol-like substance subsequently was dried at 80°C, overnight. Then, the resulting spongy and friable materials were powdered and subsequently sintered separately under an air-ambient atmosphere at temperature 200°C for 2 h. All the reagents used in this work have been purchased from Merck Inc. For convenience, a list of the abbreviations are given in Table 1. All the chemicals were purchased from Merck and used as received ones without further purification.

Physical measurements

The X-ray diffraction (XRD) patterns have been recorded using a Bruker AXS diffractometer D8 ADVANCE with Cu-K**α** radiation in the range of 2θ = 20-80° at room temperature (RT). The XRD data were analyzed using a commercial X'pert package and Fullprof program. XRD profile analysis is a simple and powerful method for evaluating the crystallite size and lattice micro-strain. Two factors determine the breadth of Bragg peak including crystallite size-dependent or strain dependent broadening effects, except instrument-dependent effect. Scherrer's equation indicates the broadening of the XRD pattern which is attributed to the crystallite size-induced broadening [10].

$$D = \frac{0.94\,\lambda}{\beta_{hkl}\cos\theta} \quad (1)$$

Here, β_{hkl} is the full-width at half-maximum of the strongest diffraction peak (311) located at about 35°. Halder and Wagner have given an approximation to the integral breadth of a Voigt function as [11]:

$$\beta_{hkl}^2 = \beta_L\beta_{hkl} + \beta_G^2 \quad (2)$$

Where β_L and β_G are the Lorentzian and Gaussian components, respectively. In cases of isotropic line broadening, the information on strain (ε) and the crystallite size (D) of the powders have been obtained from β_{hkl} and planar spacing d_{hkl} related to each reflected plane via Halder-Wagner (H-W) method [11]:

$$\left(\frac{\beta_{hkl}^*}{d_{hkl}^*}\right)^2 = \left(\frac{1}{D}\right)\left(\frac{\beta_{hkl}^*}{{d_{hkl}^*}^2}\right) + \left(\frac{\varepsilon}{2}\right)^2 \quad (3)$$

where $\beta^*_{hkl}=\beta_{hkl}\cos\theta/\lambda$ and $d^*_{hkl}=2\sin\theta/\lambda$. Finally, the results of Halder-Wagner method are compared with the Scherrer method.

The morphology of the samples was studied by the SEM (Hitachi S4160, Cold Field Emission) analysis. The FT-IR spectra of samples were recorded by using a Perkin-Elmer FT-IR spectrometer in the wave number range from 350 cm^{-1} to 2000 cm^{-1}.

Table 1: Moles of the metal nitrates for the preparation of AFe_2O_4 samples[a]

Sample	Abbreviation	Fe(NO3)3.9H2O	Cu(NO3)2.2H2O	Zn(NO3)2.4H2O	Ni(NO3)2.6H2O
$ZnFe_2O_4$	ZFO	0.050	-------	0.0170	-------
$Zn_{0.5}Cu_{0.5}Fe_2O_4$	CZFO	0.050	0.0085	0.0085	-------
$Ni_{0.3}Cu_{0.2}Zn_{0.5}Fe_2O_4$	NCZFO	0.050	0.0035	0.0085	0.0050

[a]Mole of the citric acid is considered to be 0.067 in all preparation.

RESULTS AND DISCUSSIONS

XRD analysis

XRD patterns of the $ZnFe_2O_4$, $Zn_{0.5}Cu_{0.5}Fe_2O_4$ and $Ni_{0.3}Cu_{0.2}Zn_{0.5}Fe_2O_4$ ferrites are shown in Fig. 1. Identification of structure type using X'pert high score package confirms that all the diffraction peaks of the XRD patterns can be quite well indexed to the cubic structure Fe_3O_4 (JCPDS, 74-2399) with space group Fd-3m. Therefore, all the samples are single-phase. The Miller indices have been added for all peaks in XRD pattern of ZFO.

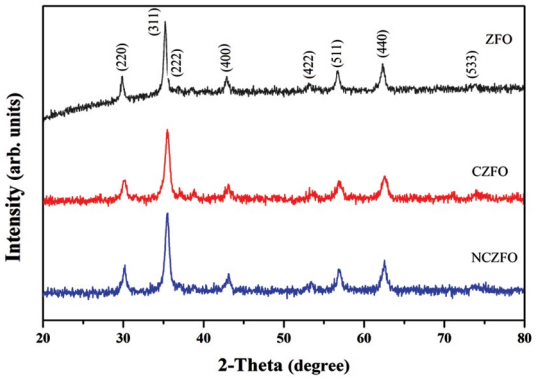

Fig. 1: X-ray diffraction pattern of ZFO, CZFO and NCZFO nanoparticles.

Accurate estimation of lattice constant has been done using Nelson–Riley (NR) extrapolation method of minimizing both systematic and random errors. The values of the lattice parameter obtained from each reflected plane related to the cubic structure were plotted against the NR function [3]:

$$F(\theta) = \frac{1}{2}\left(\frac{\cos^2\theta}{\sin\theta} + \frac{\cos^2\theta}{\theta}\right) \quad (4)$$

The extrapolation of the straight line to F(Θ) = 0 or Θ = 90° gives an accurate lattice parameter. The results are summarized in Table 2.

The X-ray density (ρ_XRD) of the samples was calculated using formula [12]:

$$\rho_{XRD} = 8M/Na^3 \quad (5)$$

Where M is the molecular weight of sample and N is the Avogadro's number. The calculated values of ρXRD are summarized in Table 2.

The theoretical lattice parameter a_{th} are obtained by the radii of tetrahedral R_A and R_B octahedral site according to the relation [13]:

$$a_{th} = 8\left[(R_A + R_o) + \sqrt{3}(R_A + R_o)\right]/3\sqrt{3} \quad (6)$$

R_0 is the radius of oxygen ion (1.32Å). R_A and R_B are the mean radius of the ions at the tetrahedral site and octahedral site. On the other hand, the mean radius of the ions at the tetrahedral site and octahedral site can also be written by cation distribution suggested in Table 2. For example, in NCZFO sample:

$$R_A = 0.5r_{Zn}^{2+} + 0.5r_{Fe}^{3+} \quad (7)$$

and the mean radius of the ions at the octahedral site is given by:

$$R_B = \frac{1}{2}[0.2\, r_{Cu}^{2+} + 0.3\, r_{Ni}^{2+} + 1.5r_{Fe}^{3+}] \quad (8)$$

Table 2: The experimental and theoretical values of lattice parameter, and also ionic radius, and cation distribution of *A*- and *B*-sites

Sample	a_{exp} (Å)	ρ(g/cm³)	R_{tetra} (Å)	R_{octa} (Å)	Cation distribution in sites		a_{th} (Å)
					tetrahedral	octahedral	
ZFO	8.500	5.214	0.600	0.645	Zn^{2+}	Fe_2^{3+}	8.196
CZFO	8.407	5.369	0.545	0.666	$Zn^{2+}_{0.5}$ $Fe^{3+}_{0.50}$	$Cu^{2+}_{0.5}$ $Fe^{3+}_{1.5}$	8.167
NCZFO	8.396	5.358	0.545	0.660	$Zn^{2+}_{0.5}$ $Fe^{3+}_{0.5}$	$Cu^{2+}_{0.2}$ $Ni^{2+}_{0.3}$ $Fe^{3+}_{1.5}$	8.151

The theoretical values of lattice parameter are calculated for the samples as summarized in Table 2. It clearly shows that the variation of theoretical lattice parameters is in good agreement with that experimental value.

In the Halder-Wagner method, the plot of $(\beta^*_{hkl}/d^*_{hkl})^2$ (axis y) versus $(\beta^*_{hkl}/d^{*\,2}_{hkl})$ (axis-x) is straight line (Fig. 2). The crystallite size is determined from the slope of the linearly fitted data and the root of the y-intercept gives the microstrain. The values of the mean crystallite size and microstrain are summurized in Table 3. The values of the positive microstrain are related to the tension stress. There are an inverse relation between the mean crystallite size and microstrain. Also, the observed increase in crystallite size of ZFO can be attributed to the increase of lattice parameter with respect to the other samples [14].

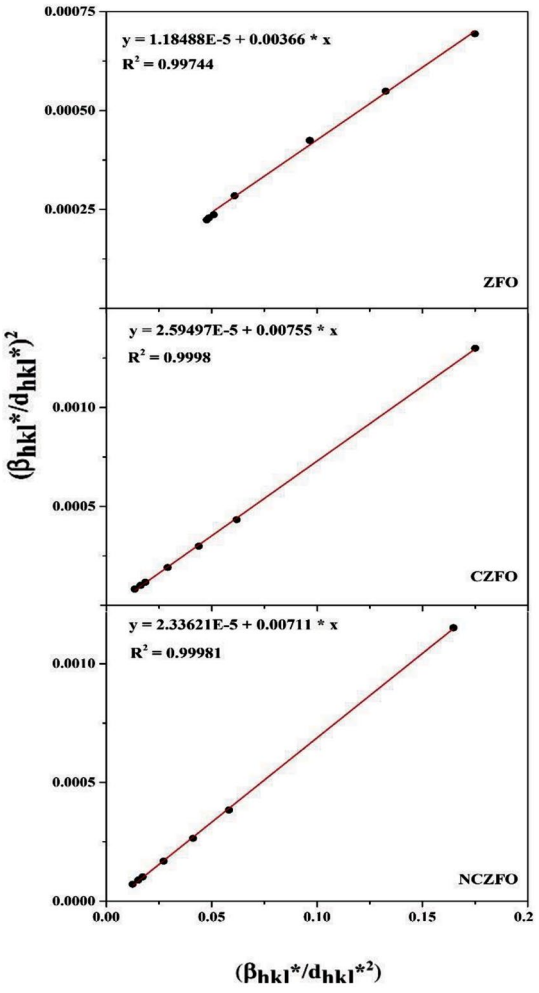

Fig. 2. Halder-Wagner plots of the ZFO, CZFO and NCZFO nanoparticles.

In the case of smaller particles, the large surface to volume ratio creates strains and distortions in the structure closer to the surface, leads to a contraction in their unit cell volume. This effect may be understood in terms of the relatively larger number of surface atoms than the atoms constituting the core of the nanoparticles. As the nanoparticles size decreases, the surface atoms will be relatively larger in number and the minimization of surface energy will necessitate the shrinking of the lattice, resulting in contraction [15]. As a result, besides the other reasons such as composition variation, we observed a higher lattice parameter for ZFO than other samples (see the values of D and a in Tables 2 and 3).

Table 3. Geometric parameters of the samples

sample #	Methods				
	Scherrer	Halder-Wagner			
	$D(nm)$	$D(nm)$	$\varepsilon \times 10^{3}$	$\sigma \times 10^{-6}$	$u \times 10^{-3}$
ZFO	22.7	27.3	6.9	844	2905
CZFO	13.8	13.2	10.9	1240	6320
NCZFO	14.7	14.1	9.7	1243	6008

FESEM analysis

The FESEM micrographs of the samples are shown in Fig. 3. The micrographs indicate the distribution of grains with non-uniform size. Also, the grains diameters observed by SEM are several times larger than the particle diameters calculated using XRD patterns, which indicates that each grain observed by FESEM consists of several particles.

IR spectra analysis

Fig. 4 shows the IR spectra of the samples. The positions of two strong bands υ_t and υ_o, written in Table 4 are related to spinel cubic structure. The band υ_t is assigned to the vibrations of the bond between the tetrahedral metal ion on A-site and the oxygen ion M_{tetra}–O. Also, the band υ_o is assigned to the vibrations of the bond between the octahedral metal ion on B-site and the oxygen ion M_{octa} – O. Therefore, the formation of spinel structure has been also

confirmed by FTIR measurement as obtained from XRD result. Looking at Table 4, we can observe that the positions of υ_t and υ_o strongly depend on the substitution ions.

The force constants for tetrahedral (K_t) and octahedral (K_o) sites were calculated employing the following equations suggested by Waldron [16]:

$$K_t = 7.62 \times 10^{-7}\, \upsilon_t^2 M_A \qquad \left(\frac{N}{m}\right) \tag{9}$$

$$K_o = 10.62 \times 10^{-7}\, \upsilon_o^2 (M_B/2) \qquad \left(\frac{N}{m}\right) \tag{10}$$

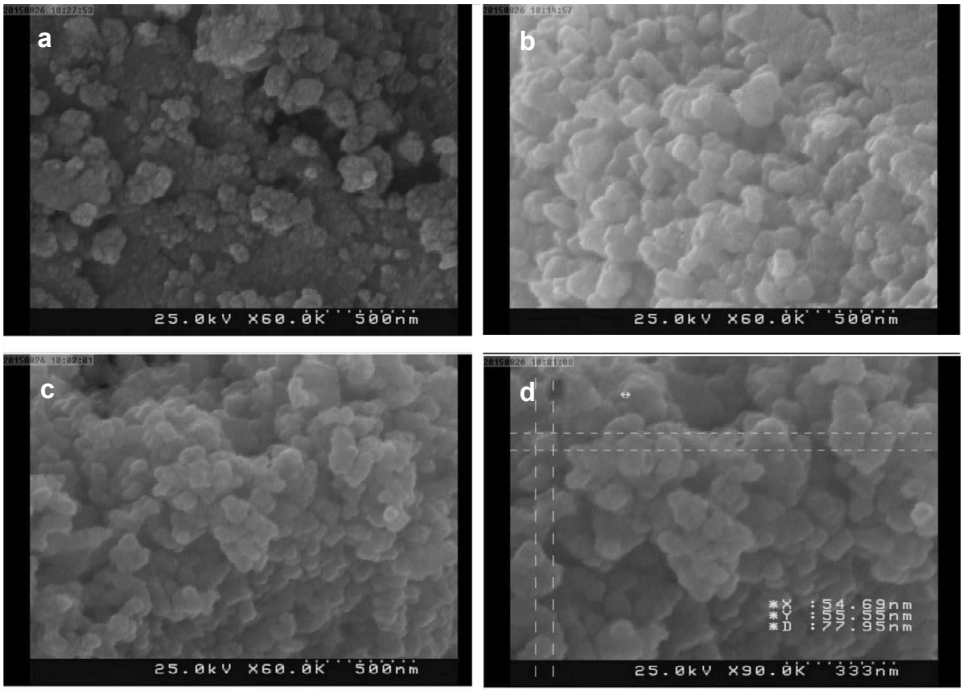

Fig. 3. FESEM micrographs for (a) ZFO (b) CZFO (c) NCZFO in scale bar 500 nm and (d) size estimation of the image (c) in scale bar 333 nm.

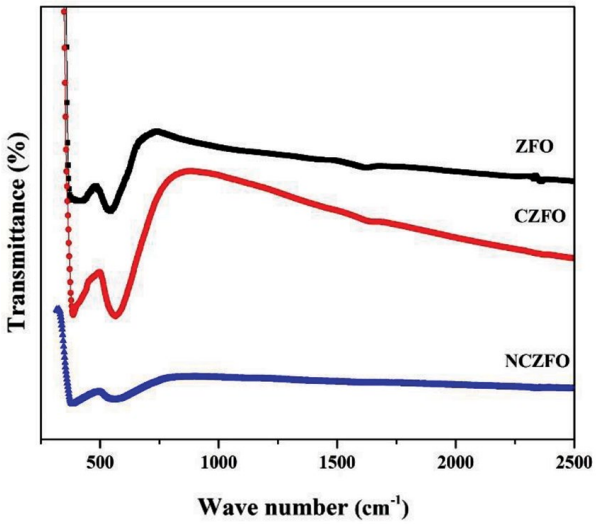

Fig. 4. FT-IR spectra of the ZFO, CZFO and NCZFO nanoparticles.

Table 4. The values of XRD density, and also vibration frequency and force constants of *A*- and *B*-sites

sample #	$\upsilon_t(cm^{-1})$	$\upsilon_o(cm^{-1})$	$K_t(N/m)$	K_o(N/m)
ZFO	535	405	147.9	97.29
CZFO	557	392	143.3	94.28
NCZFO	561	397	145.4	95.49

Where M_A and M_B are the molecular weights of cations on A- and B-sites, respectively, calculated from cation distribution formula summarized in Table 2. The calculated values for the force constants are tabulated in Table 4. These values of K_t and K_o are in the range of the values obtained by Zaki et al. [17], from far-infrared measurement of copper-zinc mixed ferrites. The values of K_t and K_o for ZFO are higher than the other samples. For the samples, the calculated value of K_t is greater than that of the corresponding value of K_o. However, the values of the bond length of *A*-site (R_{Tetra}) are smaller than those of *B*-site (R_{Octa}). This behavior can be attributed to the inverse proportionality between the bond length and the force constants [19].

For the spinel ferrite system, elastic stiffness constants and the Debye temperature can be calculated using force constants discussed elsewhere [4-6,18]. In this method, the average force constant (K) is related to the stiffness constant C_{11} by $K = a\ C_{11}$ [17], where $K = (K_t + K_o)/2$ and a is unit cell parameter. The other elastic stiffness constants of the samples have been evaluated according to the method suggested in below.

In cubic crystals, the velocity of longitudinal (V_L) and shear (V_S) waves have been calculated using the following equations [19]:

$$V_L = (C_{11}/\rho)^{1/2} \quad (11)$$

$$V_S = (C_{44}/\rho)^{1/2} = V_L/\sqrt{3} \quad (12)$$

Also, the values of V_L and V_S are used to calculate the elastic stiffness constant (C_{44}). The values of all the elastic stiffness constants are in the same ranges that are observed for the ferrites obtained by Lin et al. [20]. It is observed from Table 5 that the force constants of the ZFO are more than the other samples. This behavior can be attributed to the variation in cation-oxygen bond length [18]. Since the bond length increase, the energy required to break longer bonds is less, and this supports a decrease in the force constants.

Looking at Table 5, we can observe that the velocity of shear waves are less than longitudinal waves. This is due to when a wave travels through a material, due to the transfer of energy, it makes the particles vibrate. The vibrating particles collide with other particles which results in other particles to vibrate. In case of shear waves, the particle in a medium vibrates perpendicular to the direction of propagation of wave motion, and hence it requires a larger energy to make the neighboring particle vibrate [4]. This reduction results in the energy of waves, and hence the velocity of the shear waves is less than that of longitudinal waves. Also, the velocity of shear and longitudinal waves in the ZFO are higher than the other samples.

Table 5. The values of mean force constant, the velocity of longitudinal and shear waves, elastic stiffness constant (C_{11}, C_{44}), mean wave velocity and Debye temperature

sample #	$K(N/m)$	$C_{11}(GPa)$	$V_L(m/s)$	$V_S(m/s)$	$C_{44}(GPa)$	$V_m(m/s)$	$\Theta_D(K)$
ZFO	122.6	144.3	5260	3094	48.09	3430	487.5
CZFO	118.8	141.3	5130	3018	47.09	3345	480.2
NCZFO	120.4	143.4	5174	3043	47.81	3373	478.3

The values of V_L and V_S are used to calculate the mean wave velocity (V_m) [4]:

$$\frac{3}{V_m^3} = \frac{1}{V_L^3} + \frac{2}{V_S^3} \quad (13)$$

Next, V_m is used to calculate Debye temperature (θ_D) [5]:

$$\theta_D = \frac{h}{k_B}\left[\frac{3\rho q N_A}{4\pi M}\right]^{1/3} V_m \quad (14)$$

where h is the Plank constant, k_B is the Boltzmann constant, M is the molecular weight, q is the number of atoms in the unit formula and ρ is density. The values of V_m and θ_D are tabulated in Table 5. The decrease in the Debye temperature implies the decrease in the rigidity of the nanoparticles. It is observed from Table 5 that the Debye temperature of the ZFO is higher than the other samples. The observed variation is due to the values of IR bands observed for the samples that results the variation in strength of inter-atomic bonding as supported by our results on the variation of elastic moduli as discussed in below.

We can also use the values of V_L and V_S to calculate the longitudinal modulus (L) and the rigidity modulus (G) and then the values of Poisson's ratio (σ) that are used to calculate the elastic stiffness constant (C_{12}) as follows [4-5, 19]:

Longitudinal Modulus:

$$L = \rho(V_l)^2 \quad (15)$$

Rigidity Modulus:

$$G = \rho(V_s)^2 \quad (16)$$

Poisson's Ratio:

$$\sigma = (L - 2G)/\big(2(L - G)\big) \quad (17)$$

Stiffness constant:

$$C_{12} = \sigma C_{11}/(1 - \sigma) \quad (18)$$

The values of Poisson's ratio (σ) were found to be constant (σ = 0.2355) for the samples. Further, this value lies in the range from -0.9 to 0.5 which is consistent with the theory of isotropic elasticity [5]. The other elastic moduli for the cubic structure are calculated using the obtained constants C_{11} and C_{12} and the following relations [4-5]:

Young's modulus

$$(\mathrm{E}) = (C_{11} - C_{12})(C_{11} + 2C_{12})/(C_{11} + C_{12}) \quad (19)$$

Bulk modulus

$$(\mathrm{B}) = \frac{1}{3}(C_{11} + 2C_{12}) \quad (20)$$

The values of Young's modulus and the bulk modulus are presented in Table 6. It can be observed that the values of Young's modulus and the bulk modulus for the ZFO are higher than the other samples. Thus, it can be deduced from the increase of elastic moduli that the interatomic bonding between various atoms is strengthened.

From Uniform Stress-Deformation Model, the strain is calculated from the Hook's Law maintaining linear proportionality between stress and strain by σ = E ε, where σ is the stress of crystal and E is the modulus of elasticity or Young's modulus [19]. The energy density u (energy per volume unit) can be calculated from u = (ε²E)/2 using Hooke's law [19]. The values of stress an the energy density of the samples obtained from strain are written in Table 3.

Table 6. The values of longitudinal modulus, Poisson's ratio, elastic stiffness constant (C_{12}), Young's modulus, rigidity modulus, and bulk modulus

sample #	*L(GPa)*	*σ (unitless)*	*C_{12}(GPa)*	*E(GPa)*	*G(GPa)*	*B(GPa)*
ZFO	144.3	0.2355	44.42	123.3	49.91	77.70
CZFO	141.3	0.2355	43.51	120.8	48.89	76.11
NCZFO	143.4	0.2355	44.17	122.6	49.63	77.26

Young's modulus E(*hkl*) and Poisson's ratio $\sigma(hkl,\theta)$ are two important physical parameters of the materials and are not isotropic but depend on a specific direction in question. The general expressions for Young's modulus and Poisson's ratio along arbitrary loading direction [*hkl*] are given by the following relations for cubic crystals [19]:

$$\frac{1}{E(hkl)} = s_{11} - 2s_0 \frac{(hk)^2+(hl)^2+(kl)^2}{(h^2+k^2+l^2)^2} \qquad (21)$$

$$\sigma(hkl,\theta) = \left\{ s_{12} + \frac{s_0}{h^2+k^2+l^2} \times \left[\left(\frac{h^2 l}{\sqrt{h^2+k^2}\sqrt{h^2+k^2+l^2}} \cos\theta - \frac{hk}{\sqrt{h^2+k^2}} \sin\theta \right)^2 + \left(\frac{k^2 l}{\sqrt{h^2+k^2}\sqrt{h^2+k^2+l^2}} \cos\theta - \frac{hk}{\sqrt{h^2+k^2}} \sin\theta \right)^2 + \left(\frac{l\sqrt{h^2+k^2}}{\sqrt{h^2+k^2+l^2}} \cos\theta \right)^2 \right] \right\} / \left[-s_{11} + 2s_0 \frac{(hk)^2+(hl)^2+(kl)^2}{(h^2+k^2+l^2)^2} \right] \qquad (22)$$

where $s_0 = s_{11} - s_{12} - 1/2 s_{44}$ should be termed as the compliance anisotropy factor and $s_0 = 0$ is the condition for elastic isotropy. The three independent elastic compliances s_{11}, s_{12} and s_{44} for a cubic crystal can be calculated using the elastic stiffness constants (C_{ij}) and the following equations [19]:

$$s_{11} + 2\,s_{12} = (C_{11} + 2\,C_{12})^{-1},$$

$$s_{11} - s_{12} = (C_{11} - C_{12})^{-1},$$

$$S_{44} = 1/C_{44}\,. \qquad (23)$$

The values of s_{ij} and s_0 for the samples are summarized in Table 7.

By substituting for Miller indices of the lattice plane (*hkl*), and the values of the compliances s_{11}, s_{12} and s_{44} for the samples into equations (22) and (23), Young's modulus E(*hkl*) and Poisson's ratio $\sigma(hkl,\theta)$ along the normal direction [*hkl*] of the observed plane (*hkl*) can be obtained. Young's modulus and Poisson's ratio of the samples are summarized in Table 8. Although the values of Young's modulus E(*hkl*) for all the planes of each sample studied in this work are nearly similar to each other, but the positive values of Poisson's ratio $\sigma(hkl,\theta)$ are different. The values of Poisson's ratio (σ) were found to lie in the range from -0.9 to 0.5 which is consistent with the theory of isotropic elasticity [5]. The maximum and the minimum values of Poisson's ratio for all the samples are found along two directions [*111*] and [*110*], respectively. Here, the values of Poisson's ratio $\sigma(hkl,\theta)$ for all the planes of the samples are nearly similar, but Young's modulus E(*hkl*) is different.

Table 7. the values of s_{11}, s_{12}, s_{44} and s_0 for the samples

sample #	s_{11} $(GPa)^{-1}$	- s_{12} $(GPa)^{-1}$	s_{44} $(GPa)^{-1}$	$-s_0 \times 10^4$ $(GPa)^{-1}$
ZFO	0.0081	0.0019	0.0208	3.850
CZFO	0.0083	0.0020	0.0212	3.800
NCZFO	0.0082	0.0020	0.0209	3.500

Table 8. The values of Young's modulus (in units of *GPa*) [and Poisson's ratio] along the normal direction of the different (*hkl*) planes observed for the samples

sample #	*E*(220) [σ (220)]	*E*(311) [σ (311)]	*E*(222) [σ (222)]	*E*(400) [σ (400)]	*E*(422) [σ (422)]	*E*(511) [σ (511)]	*E*(440) [σ (440)]	*E*(533) [σ (533)]
ZFO	120.4 [0.2273]	121.5 [0.2376]	119.5 [0.2407]	123.3 [0.2343]	120.5 [0.2347]	122.5 [0.2348]	120.5 [0.2226]	120.0 [0.2301]
CZFO	118.1 [0.2299]	119.1 [0.2398]	117.2 [0.2428]	120.8 [0.2367]	118.1 [0.2370]	120.0 [0.2372]	118.1 [0.2253]	117.7 [0.2325]
NCZFO	119.4 [0.2254]	120.3 [0.2346]	118.6 [0.2375]	122.0 [0.2317]	119.4 [0.2321]	121.2 [0.2321]	119.4 [0.2212]	119.0 [0.2280]

CONCLUSION

In this work, a comparative study of X-ray peak broadening and mechanical properties in the $ZnFe_2O_4$, $Zn_{0.5}Cu_{0.5}Fe_2O_4$ and $Ni_{0.3}Cu_{0.2}Zn_{0.5}Fe_2O_4$ ferrites have been done. XRD and FTIR measurements were used to obtain the textural parameters of the materials, such as size, composition, crystal structure and also interionic binding forces and elastic moduli. The structural characterization of the samples using X'pert package is evidence for a cubic structure with space group Fd-3m. A comparative study of the crystallite size of the compounds obtained from powder XRD is reported. The Halder-Wagner analysis was used to study the individual contributions of crystallite sizes and lattice micro-strain on isotropic line broadening of the strongest reflection peaks of the samples. The values of stress and energy density have been obtained from calculated micro-strains. Also, the greater crystallite sizes of the ZFO sample with respect to the other samples can be related to the higher value of lattice parameter. The force constants for tetrahedral and octahedral sites have been determined by infrared spectral analysis. These results suggest strengthening of inter-atomic bonding on ZFO, supported by the increase in force constant, as compared to the other samples. Using the value of shear (V_S) and longitudinal (V_l) wave velocities obtained from force constants, Young's modulus (E), rigidity modulus (G), bulk modulus (B), and Debye temperature (θ_D), have been determined. The variation of elastic moduli with substitutions has been interpreted in terms of binding forces between the atoms of the spinel lattice. The values of the compliance s_{ij} and also, Young's modulus E(hkl) and Poisson's ratio $u(hkl, \theta)$ along the oriented direction [hkl] are calculated for the samples. Although the values of Young's modulus E(hkl) for all the planes of each sample studied in this work are nearly similar, Poisson's ratio σ(hkl,θ) has maximum and the minimum values along two directions [111] and [110], respectively. Here, the values of Poisson's ratio σ(hkl,θ) for all the planes of the samples are nearly similar to each other, but Young's modulus E(hkl) is different.

CONFLICT OF INTEREST

The authors declare that there is no conflict of interests regarding the publication of this manuscript.

REFERENCES

1. W. H. Bragg. The structure of the spinel group of crystals. Philosophical Magazine, 30(176) 305–315 (1915).
2. M. Ajmal, A. Maqsood. Structural, electrical and magnetic properties of $Cu_{1-x}Zn_xFe_2O_4$ ferrites (0≤x≤1). J. Alloys Compd., 460(1-2) 54–59 (2008).
3. A. Gholizadeh, E. Jafari. Effects of sintering atmosphere and temperature on structural and magnetic properties of Ni-Cu-Zn ferrite nano-particles: Magnetic enhancement by a reducing atmosphere. J. Magn. Magn. Mater., 422(1) 328–336 (2017).
4. S. G. Algude, S. M. Patange, S. E. Shirsath, D. R. Mane, K. M. Jadhav. Elastic behaviour of Cr^{3+} substituted Co–Zn ferrites. J. Magn. Magn. Mater., 350(1) 39–41 (2014).
5. S. M. Patange, S. E. Shirsath, K.S. Lohar, S. G. Algude, S. R. Kamble, N. Kulkarni, D. R. Mane, K. M. Jadhav. Infrared spectral and elastic moduli study of $NiFe_{2-x}Cr_xO_4$ nanocrystalline ferrites. J. Magn. Magn. Mater., 325(1) 107–111 (2013).
6. K. B. Modi. Elastic moduli determination through IR spectroscopy for zinc substituted copper ferri chromates. J. Mater. Sci., 39(8) 2887–2890 (2004).
7. A. Gholizadeh, A. Malekzadeh, M. Ghiasi. Structural and magnetic features of $La_{0.7}Sr_{0.3}Mn_{1-x}Co_xO_3$ nano-catalysts for ethane combustion and CO oxidation. Ceram. Int., 42(5) 5707–5717 (2016).
8. A. Gholizadeh, A. Malekzadeh. Structural and redox features of $La_{0.7}Bi_{0.3}Mn_{1-x}Co_xO_3$ nano perovskites for ethane combustion and CO oxidation. Int. J. Appl. Ceram. Technol., 14(3) 404–412 (2017).
9. A. Gholizadeh, H. Yousefi, A. Malekzadeh, F. Pourarian. Calcium and strontium substituted lanthanum manganite–cobaltite $[La_{1-x}(Ca, Sr)_xMn_{0.5}Co_{0.5}O_3]$ nano-catalysts for low-temperature CO oxidation. Ceram. Int., 42(10) 12055-12063 (2016).
10. A. Gholizadeh. $La_{1-x}Ca_xCo_{1-y}Mg_yO_3$ nano-perovskites as CO oxidation catalysts: structural and catalytic properties. J. Am. Ceram. Soc., 100 (3) 859-866 (2017).
11. A. Gholizadeh. X-Ray Peak Broadening Analysis in $LaMnO_{3+\delta}$ Nano-Particles with Rhombohedral Crystal Structure. J. Adv. Mater. Process., 3(3) 71-83 (2015).
12. A. Gholizadeh. A comparative study of the physical properties of Cu-Zn ferrites annealed under different atmospheres and temperatures: Magnetic enhancement of $Cu_{0.5}Zn_{0.5}Fe_2O_4$ nanoparticles by a reducing atmosphere. J. Magn. Magn. Mater., 452(1) 389–397 (2018).
13. G. Rana, U. C. Johri. Correlation between the pH value and properties of magnetite nanoparticles. Adv. Mater. Lett., 5(1) 280-286 (2014).
14. S. Mahmoudi, A. Gholizadeh. Effect of non-magnetic ions substitution on the structure and magnetic properties of $Y_{3-x}Sr_xFe_{5-x}Zr_xO_{12}$ nanoparticles. J. Magn. Magn. Mater., 456(1) 46–55 (2018).
15. Ch. Sujatha, K.V. Reddy, K. S. Babu, A. R. Chandra Reddy, K. H. Rao. Structural and Magnetic properties of Mg-substituted NiCuZn Nano-Ferrites. Physica B., 407(8) 1232–1237 (2012).
16. R. D. Waldron. Infrared Spectra of Ferrites. Phys. Rev., 99(6) 1727-1735 (1955).
17. H. M. Zaki, H. A. Dawoud. Far-infrared spectra for copper-zinc mixed ferrites, Physica B., 405(21) 4476–4479 (2010).
18. D. Ravinder, T. Alivelumanga. Composition dependence of elastic behaviour of mixed manganese–zinc ferrites. Mater. Lett., 37(1-2) 51–56 (1998).
19. A. Gholizadeh. A comparative study of physical properties of Fe_3O_4 nanoparticles prepared by coprecipitation and citrate methods. J. Am. Ceram. Soc., 100(8) 3577–3588 (2017).
20. J.-F. Lin, J. Wu, J. Zhu, Z. Mao, A. H. Said, B. M. Leu, J. Cheng, Y. Uwatoko, C. Jin, J. Zhou. Abnormal elastic and vibrational behaviors of magnetite at high pressures. Sci. Rep., 4(1) 6282-6287 (2014).